



**HAL**  
open science

## Role of charge carriers in long-term kinetics of polyurethane electroactuation

Gildas Coativy, K. Yuse, G. Diguët, V Perrin, L. Seveyrat, Florent Dalmas,  
Sébastien Livi, Joel Courbon, H. Takana, J. Y. Cavaille

► **To cite this version:**

Gildas Coativy, K. Yuse, G. Diguët, V Perrin, L. Seveyrat, et al.. Role of charge carriers in long-term kinetics of polyurethane electroactuation. *Smart Materials and Structures*, 2022, 31 (12), pp.125019. 10.1088/1361-665X/aca12e . hal-03955581

**HAL Id: hal-03955581**

**<https://hal.science/hal-03955581>**

Submitted on 18 Jan 2024

**HAL** is a multi-disciplinary open access archive for the deposit and dissemination of scientific research documents, whether they are published or not. The documents may come from teaching and research institutions in France or abroad, or from public or private research centers.

L'archive ouverte pluridisciplinaire **HAL**, est destinée au dépôt et à la diffusion de documents scientifiques de niveau recherche, publiés ou non, émanant des établissements d'enseignement et de recherche français ou étrangers, des laboratoires publics ou privés.

1 **Role of charge carriers in long-term kinetics of polyurethane**  
2 **electroactuation**

3 G. Coativy<sup>1</sup>, K. Yuse<sup>1,2</sup>, G. Diguets<sup>3</sup>, V. Perrin<sup>1</sup>, L. Seveyrat<sup>1</sup>, F. Dalmas<sup>4</sup>, S. Livi<sup>5</sup>, J. Courbon<sup>4</sup>,  
4 H. Takana<sup>6</sup>, J. Y. Cavaille<sup>2,7</sup>

5  
6 <sup>1</sup> Univ. Lyon, INSA-LYON, LGEF, EA682, F-69621 Villeurbanne, France

7 <sup>2</sup> Lyon Center, IFS -Tohoku U., Université de Lyon, INSAVALOR, Villeurbanne, 69621, France

8 <sup>3</sup> Advanced Institute for Materials Research, Tohoku University, 2-1-1 Katahira, Aoba-ku, Sendai  
9 980-8577, Japan

10 <sup>4</sup> Univ Lyon, INSA Lyon, UCBL, CNRS, MATEIS, UMR5510, Villeurbanne 69621, France

11 <sup>5</sup> Univ Lyon, CNRS, UMR 5223, Ingénierie des Matériaux Polymères, Université Claude Bernard  
12 Lyon 1, INSA Lyon, Université Jean Monnet, F-69623 Villeurbanne Cédex, France

13 <sup>6</sup> Tohoku Univ, Inst Fluid Sci, Aoba Ku, 2-1-1 Katahira, Sendai, Miyagi 9808577, Japan

14 <sup>7</sup> Univ Lyon, Univ Claude Bernard Lyon 1, Tohoku Univ, CNRS, INSA Lyon, Cent Lyon, ELYTMAX  
15 IRL3757, Sendai, Miyagi, Japan

16  
17 Abstract

18 Previous work has shown that dielectrophoretic body forces resulting from permittivity and conductivity  
19 heterogeneities only partially contribute to the overall electromechanical deformation of segmented  
20 polyurethanes (PUs). In this work, we studied the experimental kinetics and electric current of PU thin  
21 films over a long time period ( $1-10^5$  s) for different applied electric fields. Then, we thoroughly analyzed  
22 the drift behavior of electric carriers and its macroscopic effect using simple modeling and numerical  
23 simulation. The main assumption is that the macroscopic deformation results from the accumulation of  
24 electric charges near the electrodes, leading to local stretching. Assuming that the mobilities of negative  
25 and positive carriers are different, their migration towards the electrodes will have different kinetics. A  
26 preliminary simulation attempt using a single set of parameters, supports these assumptions, and leads  
27 to a correct bending amplitude and current evolution according to the applied electric field. Furthermore,  
28 the resulting compression is consistent with the observed electrostriction.

29

30 Keywords: Polyurethane; Electroactive Polymer; Bending, Simulation; Electric Current, Polymer

31

## 1. Introduction

Recent decades have been marked by the design and development of actuators based on electroactive polymers (EAPs), which can even be used to replace piezoelectric ceramics or shape memory alloys [1,2]. Numerous applications can be found in soft robotics and biomimetics [3–5]. EAPs consist of thin polymer films covered with flexible electrodes. Dielectric elastomers are very attractive as EAPs owing to their light weight, flexibility, low cost, ease of implementation, and large electric field-induced strain [6]. Though many studies have been conducted on the actuating performance, the origin of the electromechanical strain remains controversial and unclear, especially for polyurethane (PU) electronic EAPs [7,8]. This thermoplastic polymer with its unique microphase separation is a promising candidate for actuator and sensor applications thanks to its dielectric and mechanical performances, and tunable properties through composition control depending on the fillers used [9–12].

PU materials can be stimulated in compression (reduction of thickness) or in bending (with a fixed end and a free end) by an electric field. In compression, the strain is proportional to the square of the electric field as follows:

$$S = ME^2, \quad (1)$$

where  $M$  is the electroactivity coefficient, which includes different contributions such as the mutual attraction of oppositely charged electrodes [12,13], and the orientation and attraction of the constitutive dipoles or phases of the material [12,13]. The coefficient  $M$  is linked to the dielectric and mechanical properties of the material and is generally supposed to be time-independent. However, the electro-action time scale under compression is much longer than the mechanical and dielectric time scales [7,14]. In addition, the contributions above cannot describe the bending behavior of such PUs when subjected to an electric field.

Regarding PU compression, a model involving dielectrophoretic force was proposed to bring a time dependency to deformation [7]. However, the amplitude of the obtained time-dependent solution is not sufficient to describe the whole phenomenon [7]. Furthermore, PU bending suggests an asymmetric process that is not involved in the simple electric field-induced deformation when dipole orientation and charge distributions are symmetric [15,16]. EAP bending is generally described for wet polymers as coming from the displacement and accumulation of liquid molecules near the electrodes (steric stress), and for dry polymers as resulting from a heterogeneous distribution of charges inside the films, which produces Coulombic forces (electrostatic pressure) [16–18]. Therefore, another mechanism based on charge carrier drift could explain both the time dependency of electro-actuation and the asymmetric process involved in PU bending.

It has already been shown that the origin of charge carriers in PU may be ionic impurities [19–21] already present in the polymer matrix or charge injection [22–24]. The polarization and conduction

67 mechanisms in polymers such as the studied PUs are very complex. In addition to the dipolar relaxations  
68 due to the presence of permanent dipole moments, phenomena such as interfacial polarization, which  
69 occur at the internal interfaces in heterogeneous and DC conduction, should be considered especially  
70 for long periods of time. In PU, it was already highlighted that the hard and soft domains exhibit different  
71 dielectric and conductive properties, which is favorable to interfacial polarization. Wongtimnoi et al.  
72 [25] found a decrease of the DC conductivity with increasing hard domains fraction. Pissis [26] indicated  
73 also that  $\sigma_{DC}$  decreases with increasing hard domains content, suggesting that charge carrier transport  
74 occurs mainly through the soft domains. They described an accumulation of charges at the interfaces  
75 between regions of different conductivity. Charges and ions can be moved and trapped in an electric  
76 field. Dielectric spectroscopy studies conducted on the same PU used in this study have found activation  
77 energies for DC conductivity of about 0.6 eV, which favors an ionic origin for the conduction  
78 [27]. Charge carrier drift could be responsible for the complex kinetics of actuation and its bending  
79 [28,29]. However, to our knowledge, the study of coupling of PU bending to electric current has been  
80 limited to a few hundred seconds [15]. Therefore, the aim of this work is to investigate the electro-  
81 actuation of thin PU films over a long time ( $10^5$  seconds) under a constant applied electric field and  
82 attain a better understanding of possible mechanisms behind such long kinetics based on a first  
83 simulation attempt.

84

## 85 2. Materials and methods

86

87 The polymer films were prepared by solvent casting. PU pellets (Estane 58887 NAT038 Lubrizol,  
88  $1.13 \text{ g}\cdot\text{cm}^{-3}$ , 87 shore A) were used. This block copolymer is composed of 4,4-methylene diphenyl  
89 diisocyanate and 1,4-butanediol hard segments, and poly(tetramethylene) oxide (PTMO) soft segments.  
90 The pellets were first heated at  $100 \text{ }^\circ\text{C}$  for 3 hours and then dissolved in N,N-dimethylformamide (DMF,  
91 Honeywell D158550) with a concentration of 20 wt% PU in DMF. To obtain a homogeneous solution,  
92 the mixture was heated in a closed system under reflux at  $80 \text{ }^\circ\text{C}$  for 3 hours under mechanical stirring.  
93 This system ensures there is no solvent evaporation. The solution was then transferred to a closed jar  
94 and left aside for 24 hours to get rid of the bubbles left in the viscous solution.

95 PU films were then fabricated by tape casting. The solution was cast on glass plates by an Elcometer  
96 3700 doctor blade film applicator, then put in an oven at  $60 \text{ }^\circ\text{C}$  for 20 h, and then removed from the  
97 glass. A second heating treatment at a temperature below the melting temperature was performed to  
98 eliminate the residual DMF solvent. The thickness of the films was  $100 \text{ }\mu\text{m}$  after the thermal treatments.  
99 The films were then soaked in a saturated solution consisting of 30 wt% NaCl (sodium chloride 99.5–  
100 100.5%, AnalaR NORMAPUR - Reference 27810.295, Aldrich) in distilled water for 3 days to ensure  
101 complete penetration of the salt into the PU. A drying step was then applied at  $100 \text{ }^\circ\text{C}$  for 2 hours to  
102 eliminate the water. The films were cut into rectangular samples with a length of 35 mm and width of 6  
103 mm. A thin gold layer was deposited on each face of the samples with a sputter coater (Cressington

104 208HR, US). The thickness of the gold layer was about 20 nm. The samples were then put in a desiccator  
105 with a constant humidity of 59% (at a temperature of 20–22 °C). After a 2-weeks storage period, the  
106 samples were used for measurements.

107 The conductivity was measured at room temperature with a Schlumberger Solartron 1255  
108 impedance/gain phase analyzer and a 1296 dielectric interface under an AC voltage of 1 V rms at 0.1  
109 Hz.

110 The experimental setup for bending measurement was in a closed chamber with controlled humidity  
111 (57–59%) at a temperature of 20–22 °C. During the experiment, it was checked that the temperature of  
112 the material did not change significantly using an IR camera. The sample was clamped in a designed  
113 sample holder with copper tracks and vertically hung. The free part of the sample was 25 mm in length.  
114 Figure 1 shows the setup used to measure the free-end displacement  $d$  of the sample.

115 A DC electric field (voltage step) was applied to the sample using a function generator (Keysight  
116 33220A, US) and a voltage amplifier (TREK 609D-6, US). The current was measured through a current  
117 amplifier (Stanford SR570, US).

118 The displacement was measured through a laser sensor (Keyence head LK-H052, controller LK-  
119 G5001PV, Japan). Signals (voltage, current, displacement) and ambient parameters (temperature,  
120 humidity) were recorded through a Dewesoft data acquisition system over a long time (4 to 15 hours).  
121 Displacement was positive when the film bent toward the high-voltage (HV) direction and negative  
122 when it moved toward the ground direction (figure 1).

123  
124

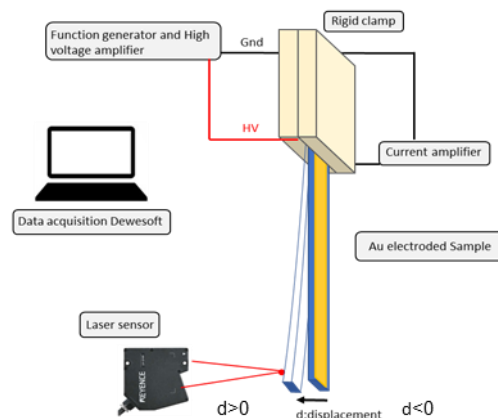


Figure 1: Experimental setup of the bending test. The bending displacement  $d$  is positive when the end of the sample goes to the positive voltage.

125  
126  
127

128 3. Experimental results

129

130 The first bending experiment was carried out over 15 hours on a sample subjected to an electric field  
131 of 10 MV/m to observe its complex bending kinetics. Then, a series of experiments was performed over  
132 4 hours on samples stabilized with the protocol described in the previous section under different electric  
133 fields: 2, 4, 6, 8, and 10 MV/m.

134

135 3.1 Kinetics of PU displacement under a constant applied electric field over 15 hours

136 Figure 2 shows the bending displacement  $d$  and current density  $j$  of a PU sample stimulated by  
137 a constant electric field of 10 MV/m. During the first tens of seconds, the current density is constant and  
138 equal to  $j=8.3\times 10^{-3}$  A/m<sup>2</sup>. During this period, the displacement is also constant and equal to  $d=0$   $\mu\text{m}$ .  
139 Then, the displacement goes in the ground direction to reach a minimum displacement of  $d=-3000$   $\mu\text{m}$ ,  
140 changes its direction, and tends almost to zero after 15 hours. The current density continuously decreases  
141 and loses two logarithmic decades in 15 hours. This experiment shows the complex kinetics of PU  
142 bending that extends over five logarithmic decades of time in seconds. It also highlights a link between  
143 current and displacement: during the first tens of seconds, current and displacement are constant, and  
144 they evolve after. In contrast to the current density, the displacement is non-monotonic, i.e. the free end  
145 of the PU film first goes in the ground direction and then returns to zero. Interestingly, this result  
146 suggests a competition between two opposite effects with the same amplitude but different kinetics. The  
147 origin of such a behavior could be the successive migration and accumulation of anions (negative  
148 charges) and cations (positive charges) near the positive and negative electrodes, respectively. The fact  
149 that the displacement returns to zero suggests that the same number of anions and cations is present in  
150 the material, while the observation of a non-zero displacement for intermediate times requires that their  
151 mobility is different.

152

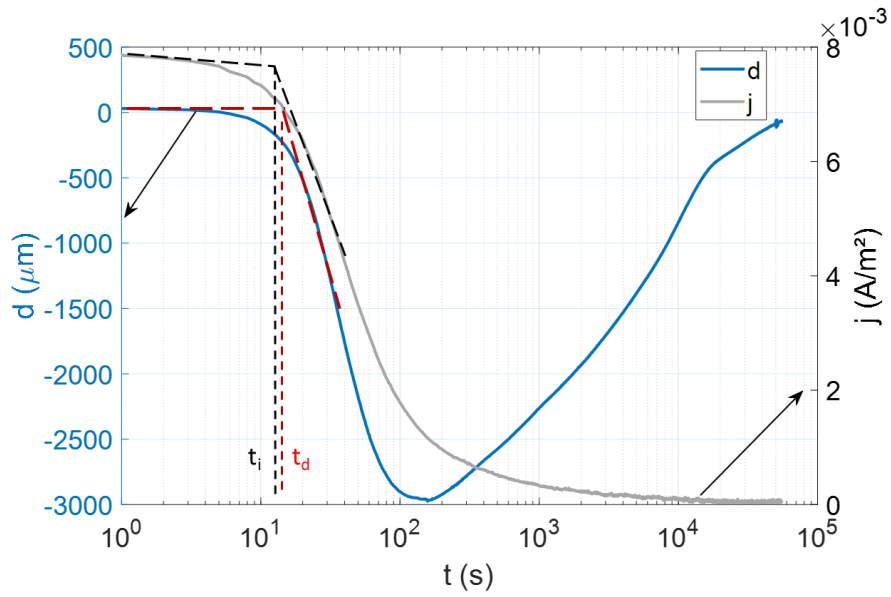


Figure 2: Displacement and current density for a sample subjected to a continuous electric field  $E=10$  MV/m over 15 hours ( $t_d$  and  $t_i$  are the times at which the displacement and the current density start to decrease, respectively).

153

### 154 3.2 Effect of the electric field on bending and current responses

155

156 The electro-actuation of PU was evaluated under different applied electric fields: from 2 to 10  
 157 MV/m for 4 hours. The current density and displacement versus time are plotted in figure 3.

158

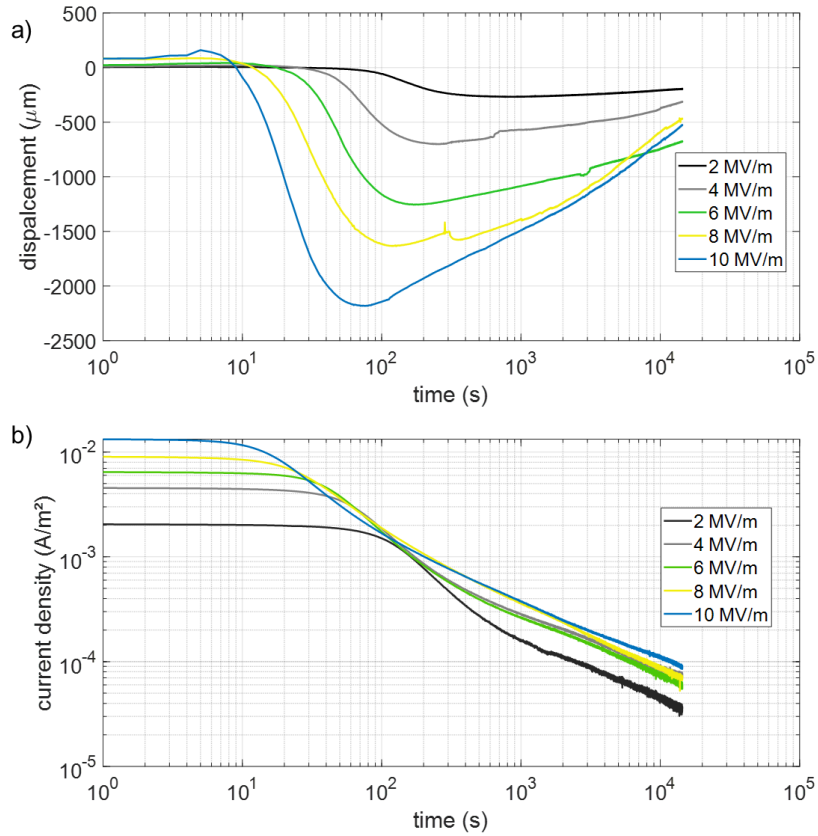


Figure 3: a) Bending displacement of the free end of the sample and b) current density for samples subjected to different constant applied electric fields (2, 4, 6, 8, and 10 MV/m) as functions of time.

159

160 First, we notice that the displacement and current density curves all have the same shape, but  
 161 the kinetics and amplitude vary. The length of the initial plateau changes from several hundred seconds  
 162 to a few seconds as the electric field increases from 2 MV/m to 10 MV/m. The initial current density  $j$   
 163 and the absolute value of displacement  $|d|$  increase as the applied electric field increases. The initial  
 164 value of  $j$  is plotted in figure 4 as a function of the applied electric field  $E$ . It shows a linear relationship  
 165 up to an applied electric field of 8 MV/m with a slope  $\sigma=1.2\times 10^{-9}$  S/m over the same range of values as  
 166 when measured at low electric field with the dielectric spectrometer ( $\sigma=4\times 10^{-10}$  S/m). This suggests that  
 167  $\vec{j} = \sigma\vec{E}$  and thus that the current follows Ohm's law involving charge carriers probably coming from  
 168 ionic species. In the case of charge injection in a dielectric elastomer, the current density should not  
 169 follow a linear relationship with the applied electric field [22,30].

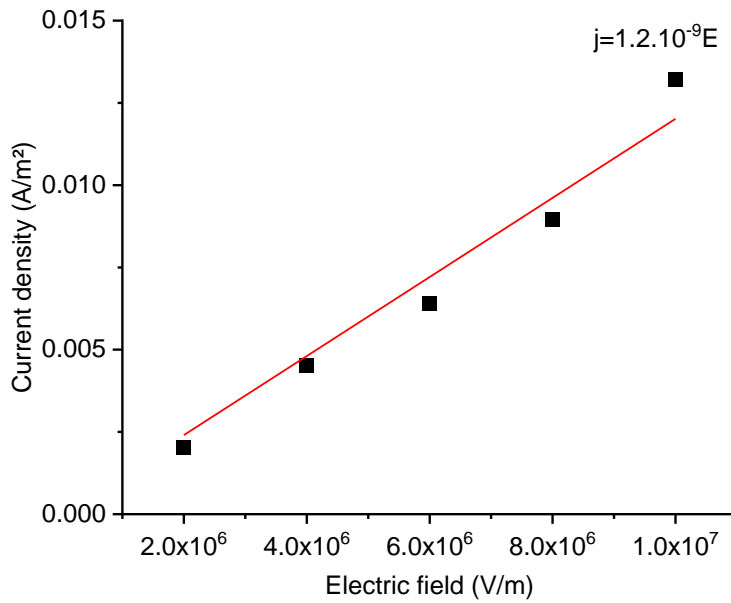


Figure 4: Initial current density  $j$  as a function of applied electric field  $E$ .

170 Finally, the natural logs of  $t_i$  and  $t_d$  (figure 2), the times at which the displacement  
 171 density start to decrease, are plotted as functions of the electric field in figure 5. The natural log of each  
 172 time response decreases linearly when the applied electric field increases. Further work is required for  
 173 a better understanding of this result.

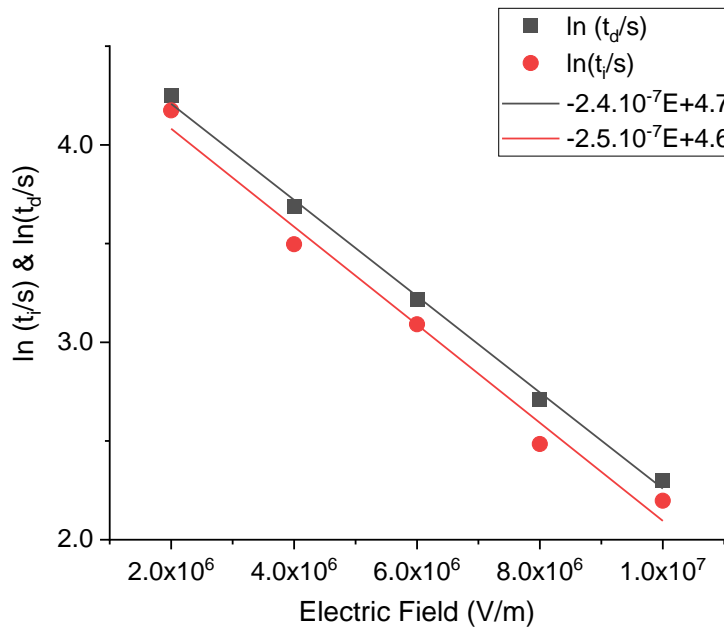


Figure 5: Natural log of onset of bending displacement ( $t_d$ ) and onset of current decrease ( $t_i$ ) as functions of the applied field  $E_0$ .

175 4. Modeling and simulation

176 4.1 Modeling

177 Most models and simulations of the bending of electroactive polymers deal with wet or dry  
178 IPMC with a free cation and an anion attached to the polymer backbone [17,31,32] or dielectric elastomer  
179 bonded to a substrate (with different Young's modulus and dielectric permittivity) [8,33]. Although these  
180 simulations work well, they are not representative of our experiment as no substrate is present and the  
181 sample is not an IPMC. An analytical model based on charge injection has already been successfully  
182 developed for PU [23]. However, Le Roy et al. propose that in a dielectric material, the charge carriers  
183 can be ionic charge carriers from salt dissociation and electrons and holes from charge injection [34]. In  
184 our case, we propose a simulation based on the presence of only two types of ions with opposite charges  
185 and different mobilities. The two types of charges taken into account here correspond mainly to  $\text{Na}^+$  and  
186  $\text{Cl}^-$  from the immersion of the sample in a salt water bath. The simulation can then be enriched in a  
187 future work by adding the presence of electrons and holes. The main assumption is that the macroscopic  
188 deformation results from accumulation of electric charges near the electrodes. Assuming that the  
189 mobilities of negative and positive carriers differ, their migrations towards the electrodes follow  
190 different kinetics.  
191

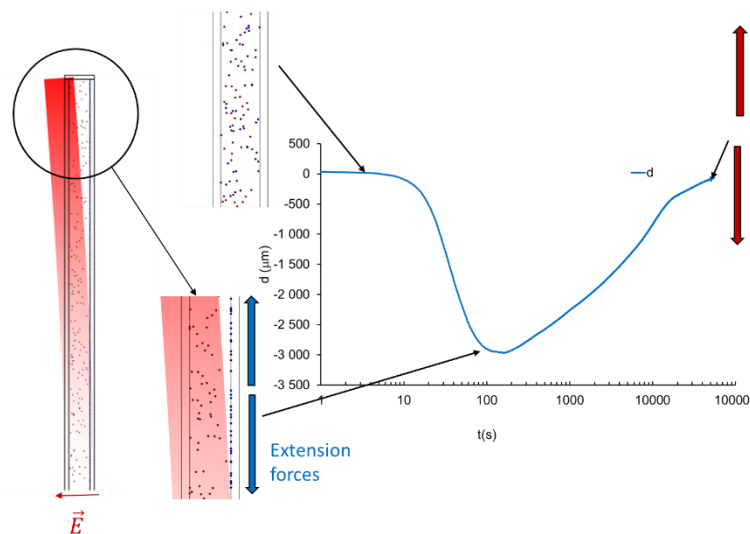


Figure 6: Schematic scenario in which blue particles move to the right faster than red particles move to the left. Owing to their repulsive forces, the thin sample bends first to the left and then to the right. In the end, we expect the sample to stretch.

192 The repulsive forces near the electrodes due to ion accumulation induce elongation of the  
193 surface, which in turn causes the sample to bend, assuming there are no equivalent forces near each  
194 opposite electrode. For a period of time long enough to allow for migration of all electrical charges, the

195 bending can be expected to (i) go through a maximum and then (ii) return to zero. The scenario is  
 196 illustrated in figure 6. In the case where a species cannot move (e.g. when ions are bound to  
 197 macromolecules), only the mobile charges play a role and induce permanent curvature under the electric  
 198 field.

199 In the following part, the polymer is considered differently depending on the scale considered.  
 200 As a macroscopic material, it behaves like an elastic solid because of its rubbery state. At a nanoscopic  
 201 level, i.e. the scale of electric charges, it behaves like a viscous liquid, allowing the charges to drift over  
 202 long distances. Clearly, this behavior is far from Newtonian in polymers, and has been discussed  
 203 considering the diffusion of molecules or atoms in a polymer network [35,36]. The electric carriers in  
 204 the following theory are considered as particles.

205 The general idea is that each charged particle is subjected to two main forces that depend on its position  
 206  $\vec{r}$  and on time  $t$ . The first is the electric force,

$$\vec{f}_E(\vec{r}, t) = q\vec{E}(\vec{r}, t), \quad (2)$$

207 where  $q$  is the electric charge in C, and  $\vec{E}$  is the local electric field in V/m. The second force is a dragging  
 208 force due to the interaction of the particles moving in the surrounding viscous medium:

$$\vec{f}_{p,n}^{drag}(\vec{r}, t) = -k\vec{v}_{p,n}(\vec{r}, t), \quad (3)$$

209 where  $k$  is a constant related to the shape of the particle and to the surrounding apparent viscosity, and  
 210  $\vec{v}$  is the velocity of a positive (subscript  $p$ ) or negative (subscript  $n$ ) charged particle. We can also  
 211 introduce the electrical mobility  $\mu$ , which relates the velocity and local field when the limit velocity is  
 212 reached:

$$\begin{aligned} \vec{v}_p(\vec{r}, t) &= \mu_p\vec{E}(\vec{r}, t) = \frac{q}{k}\vec{E}(\vec{r}, t), \\ \vec{v}_n(\vec{r}, t) &= -\mu_n\vec{E}(\vec{r}, t) = -\frac{q}{k}\vec{E}(\vec{r}, t). \end{aligned} \quad (4)$$

213  
 214 In the following, we consider a thin film having a thickness  $W$  and coated by two electrodes,  
 215 one at  $x=-W/2$  and the other at  $x=W/2$  (figure 7). For simplicity, we will consider the main component  
 216 of  $\vec{E}$  to be perpendicular to the film plane and denote it as  $E$ . Before the electric field is applied, one set  
 217 of positive particles and another set with an equal number of negative particles are randomly dispersed  
 218 inside the film. At  $t=0$  s, the field is applied with a uniform strength  $E=E_0$ . Under the electric force, the  
 219 particles move towards the electrodes according to their sign. These motions induce a local electric field  
 220 opposite to the applied electric field. The resulting local field decreases with time and is a function of  
 221 both the position  $x$  and time  $t$  [ $E(x,t)$ ].

222 For the region near each electrode, it is then possible to write

$$\begin{aligned} E_1(t) &= E_0 \left(1 - \frac{n_p(t)}{N_S}\right), \\ E_2(t) &= E_0 \left(1 - \frac{n_n(t)}{N_S}\right), \end{aligned} \quad (5)$$

223 where  $E_1(t) = E(-W/2, t)$ ,  $E_2(t) = E(W/2, t)$ ,  $N_S$  is the number of particles leading to zero local field,  
 224 and  $n_n(t)$  and  $n_p(t)$  are the numbers of negative and positive particles frozen on the electrodes at time  
 225  $t$ . The number  $N_S$  can be evaluated considering that a uniformly charged plane produces an electric field  
 226  $E_i$  (perpendicular to the plane) equal to

$$E_i = \frac{\sigma_S}{2\varepsilon_r\varepsilon_0} = \frac{qn_{p,n}}{2\varepsilon_r\varepsilon_0S}, \quad (6)$$

227 where  $\sigma_S$  is the surface charge density,  $\varepsilon_r\varepsilon_0$  is the dielectric permittivity around the plane, and  $S$  is the  
 228 electrode surface area. Thus,  $N_S = \frac{2E_0\varepsilon\varepsilon_0S}{q}$ . It is noteworthy that if the total number of carriers,  $N_{tot}$ , is  
 229 larger than  $N_S$ , then the field near the electrode becomes 0 and so does the carrier velocity, leaving a  
 230 constant local charge density.

231 In the bulk, we assume for simplicity that the field follows a linear dependence on the particle  
 232 position  $x$  between the two electrodes (figure 7):

$$\begin{aligned} E(x, t) &= a(t)x + b(t) \\ \text{with } a(t) &= \frac{E_2(t) - E_1(t)}{W} \\ \text{and } b(t) &= \frac{E_2(t) + E_1(t)}{2}. \end{aligned} \quad (7)$$

233

#### 234 4.2 Current density kinetics

235 The current density  $j(t)$  can be evaluated from the number of charged carriers still free in the  
 236 dielectric material, accounting for their number and velocity:

$$j = \sum_i^{N_{tot}} \frac{n_i}{V} q_i v_i. \quad (8)$$

237 We should point out that the initial current ( $t=0$ ) is directly triggered by  $N_{tot}$  and depends on the charge  
 238 and initial velocity of each carrier.

239

#### 240 4.3 Bending evaluation

241 As mentioned above, the bending results from the repulsive forces between the electric charges,  
 242 whose density varies in time during their migration to the electrodes. Owing to the difference in mobility  
 243 between the positive and negative charges, the force field is not symmetric, which induces the observed  
 244 bending. The local charge density changes with time assuming that the carriers reach the vicinity of the  
 245 electrodes and remain in a thin layer [21], resulting in a local electrostatic energy  $W_E(r, t)$ . Thus, the force  
 246 field can be derived as

$$\overrightarrow{f}(r, t) = -\overrightarrow{\nabla}W_E(r, t), \quad (9)$$

247 where  $r$  refers to the position in space. The corresponding deformation is easily calculated using a finite  
 248 element code, as discussed below.

249 4.4 Numerical simulation

250 Because the local electric field depends on both time and position, it is really difficult to derive  
 251 analytical functions that provide the evolution of the current and the bending deflection versus time. We  
 252 therefore used the software COMSOL Multiphysics and implemented the modules “Electrostatics,”  
 253 “Charged Particle Tracing,” and “Solid Mechanics”. To reduce the computational time, our calculations  
 254 were performed in a 2D representation. The simulated sample (figure 7) consists of a ribbon of tree-like  
 255 layers with a main layer (core) of thickness  $W$ , and two thin layers (thickness  $e$  with  $e \ll W$ ).

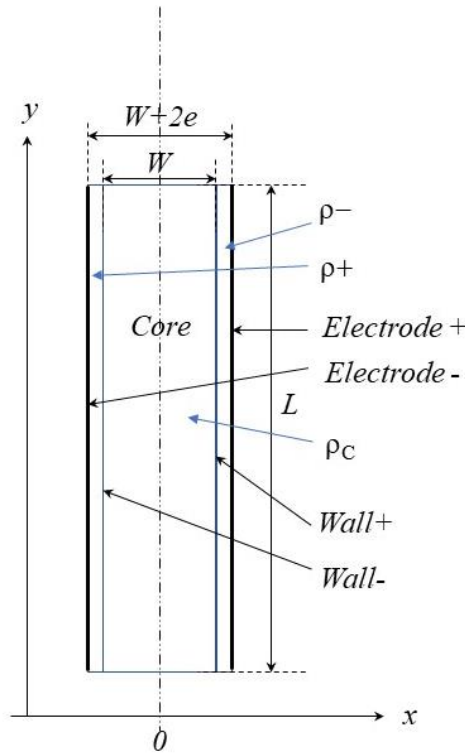


Figure 7: Schematic of a typical sample used for the COMSOL simulation.

256 The boundaries between the core and the thin layers are called Wall+ for the layer closest to the  
 257 + electrode, and Wall- for the other one. The outer boundaries are iso-potential surfaces corresponding  
 258 to the applied voltage. The “Charge Particle Tracing” module is mainly used for the kinetic aspect of  
 259 the simulation, while “Electrostatics” provides the local field and electrical energy. “Solid Mechanics”  
 260 is used to calculate the force and strain fields in the simulated sample. Because the number of charge  
 261 carriers is limited, each carrier has a charge  $Z$  much higher than that of one electron.

262 All parameters are listed in table 1.

263 The simulation combined both electricity and solid mechanics using a time-dependent solver.  
 264 For the electrical part, we chose to study the drift of electrical carriers subjected to the local electric  
 265 field. Thus, positive and negative carriers were subjected to two forces, a Coulombic force and a  
 266 dragging force, which tends to limit their velocity in a steady state. This corresponds to assigning  
 267 mobilities  $\mu_p$  and  $\mu_n$  to positively and negatively charged carriers, respectively [equation (4)]. Initially,

268 a set of these positive and negative carriers are randomly distributed in the core of the sample, and the  
 269 average electric charge is zero. To avoid instabilities at the beginning of the simulation, the field is  
 270 gradually increased and reaches its constant value at  $t=1$  s. This is comparable to the experimental  
 271 conditions we used for our measurements.

272 As each charged particle moves towards the electrode with the opposite sign, it reaches Wall+  
 273 and Wall- and remains blocked. Its electric charge is added as a charge density increment in the layer  
 274 near the wall, and is subtracted from that of the core.

275 As the two layers experience different kinetics in terms of their charge density variations, we  
 276 propose that the space charge density  $\rho_C(x, t)$  is not homogeneous inside the core, but follows a gradient  
 277 such as

$$\rho_C(x, t) = [a(t)x - b(t)] \frac{e}{W} \quad (10)$$

$$\text{with } a(t) = \frac{\rho_-(t) - \rho_+(t)}{W}$$

$$\text{and } b(t) = \rho_+(t) + \rho_-(t),$$

278 where  $\rho_-(t)$  and  $\rho_+(t)$  are the space charge densities of the two layers (figure 7). This insures that the  
 279 total electric charge in the whole sample remains zero.

280 As a result, the field near each wall decreases each time a carrier reaches this wall, which slows the  
 281 velocity of the particle depending on the local value of  $E(x, t)$  [equation (7)]. At each time step, the local  
 282 energy density is calculated and the local force field is derived according to equation (9). The Solid State  
 283 Mechanics module makes it easy to calculate the change in shape of the sample.

284 Several remarks have to be made:

- 285 1. First, it is far from possible to implement an electric carrier number  $N_{tot}$  comparable to that of  
 286 the real situation. For this reason, we chose  $N_{tot}$  to be  $3 \times 10^4$  particles, which is a good  
 287 compromise for optimizing the simulation duration and the numerical noise in the calculated  
 288 data. The parameters in table 1 were determined to fit the maximum bending amplitude obtained  
 289 from our experiments for an applied field of  $10^7$  V/m. This leads to an electric charge per carrier  
 290 of  $2 \times 10^8 ec$ , where  $ec = 1.6 \times 10^{-19}$  C.  
 291
- 292 2. The size of the mesh depends on the size of the domains. The smallest dimension in our model  
 293 is determined by the thickness of the lateral layer, in this case,  $2 \mu\text{m}$ . Because the computation  
 294 time is directly related to the number of cells, we considered a simulated sample whose length  
 295 is equal to one tenth of that of a real sample. Thus, on the basis of previous work, the expected  
 296 bending displacement should be equal to one hundredth of that measured on a real sample [23].  
 297 Meanwhile, the calculated current should be equal to one tenth of that measured in the real  
 298 sample. These two factors (10 for the current and 100 for the bending displacement) are applied

299 to the simulation results presented below. Within this framework, the number of cells was less  
 300 than 30,000.

301

302 3. Effect of the lateral layer thickness. As discussed above, the mesh is thinner when the two layers  
 303 are thinner, and the calculation time is longer. We performed a series of simulations considering  
 304 layer thicknesses ranging between 1  $\mu\text{m}$  and 10  $\mu\text{m}$ . The results remain unchanged for layers  
 305 thinner than 3  $\mu\text{m}$ , so we decided to choose 2  $\mu\text{m}$  as a good optimization.

306

307 Table 1: Parameter values used for the COMSOL simulation. The only parameter that was varied was  
 308 the applied voltage corresponding to that in the experiments.

Term	Quantity	Value
$V_0$	Applied voltage	200 to 1000 kV
<i>Thickness</i>	Sample thickness ( $W+2e$ )	100 $\mu\text{m}$
$E_0$	$V_0/(W+2e)$	$0.2 \times 10^7$ to $1.2 \times 10^7$ V/m
$\mu_n$	Fast particle mobility	$3 \times 10^{-14}$ $\text{m}^2/(\text{s.V})$
$\mu_p$	Slow particle mobility	$3 \times 10^{-16}$ $\text{m}^2/(\text{s.V})$
$W$	Core thickness	96 $\mu\text{m}$
$L$	Sample length	2.5 mm
$L$	Sample width	6 mm
$E$	Layer thickness	2 $\mu\text{m}$
$Z_0$	Electric charge per positive carrier	$1 \times 10^8$ $ec$
$-Z_0$	Electric charge per negative carrier	$-1 \times 10^8$ $ec$
$N_{tot}$	Total number of positive (and negative) carriers	30000
$Y_M$	Young modulus of the sample	40 MPa
$\epsilon$	Dielectric constant of the sample	8
<i>Mesh</i>	Number of mesh elements	26050

309

#### 310 4.5 Comparison between experimental and simulation data

311 Figure 8 shows both the experimental and simulated curves of displacement and normalized  
 312 current. It also highlights the simulated longitudinal displacement (orthogonal to the  $x$  axis) and the  
 313 resulting compressive strain deduced using a Poisson coefficient of approximately 0.5. Simulation  
 314 parameters such as ionic mobility have been optimized for a field  $E_0 = 10^7$  V/m, and all parameters  
 315 remain unchanged for all other values of  $E_0$ .

316 As previously mentioned, the calculated short-term current (in our case,  $t=1$  s), depends on (i) the  
 317 number of carriers and their electric charge, (ii) their mobility, and (iii) the applied electric field.

318 Meanwhile, the bending displacement depends on the gradient of the electric energy density, which in  
319 turn depends on (i) the local electric charge density, (ii) the ratio between the slow and fast mobilities  
320 of the carriers, and (iii) the applied field.

321 The simulated bending displacement evolves over  $10^4$  s but starts and finishes earlier than the  
322 experimental one. The amplitude for each applied electric field is on the same order of magnitude as the  
323 experimental amplitude. However, for an electric field below 10 MV/m, the simulated bending  
324 displacement amplitude is systematically lower.

325 The current that we obtained from these simulations is about one hundredth of the measured one,  
326 and it shows two processes due to the difference in mobility between the two types of charge carriers. It  
327 is noteworthy that while the bending results from the competition between the diffusions of carriers with  
328 opposite signs, the current is the sum of all diffusing carriers. This means that if we have many more  
329 carriers with intermediate mobilities, they will not play any role in the bending, but will all contribute  
330 to the current. In fact, Watanabe et al. [19] have shown that PU contain impurities that contribute to  
331 their conductivity. To remove their contributions, further investigations is needed with model samples  
332 in which we can control the number of carriers and their mobilities within the polymer. This work is in  
333 progress.

334 An overall stretch is expected because the bending of the sample results first from the elongation  
335 of the material near one electrode followed by a similar elongation near the second electrode. This is  
336 shown in figure 8c: the calculated elongation reaches  $16\ \mu\text{m}$  for an applied potential of 1000 V (i.e. for  
337  $E_0=10$  MV/m) for a sample length of 25 mm, corresponding to a deformation of approximately 0.06%.

338

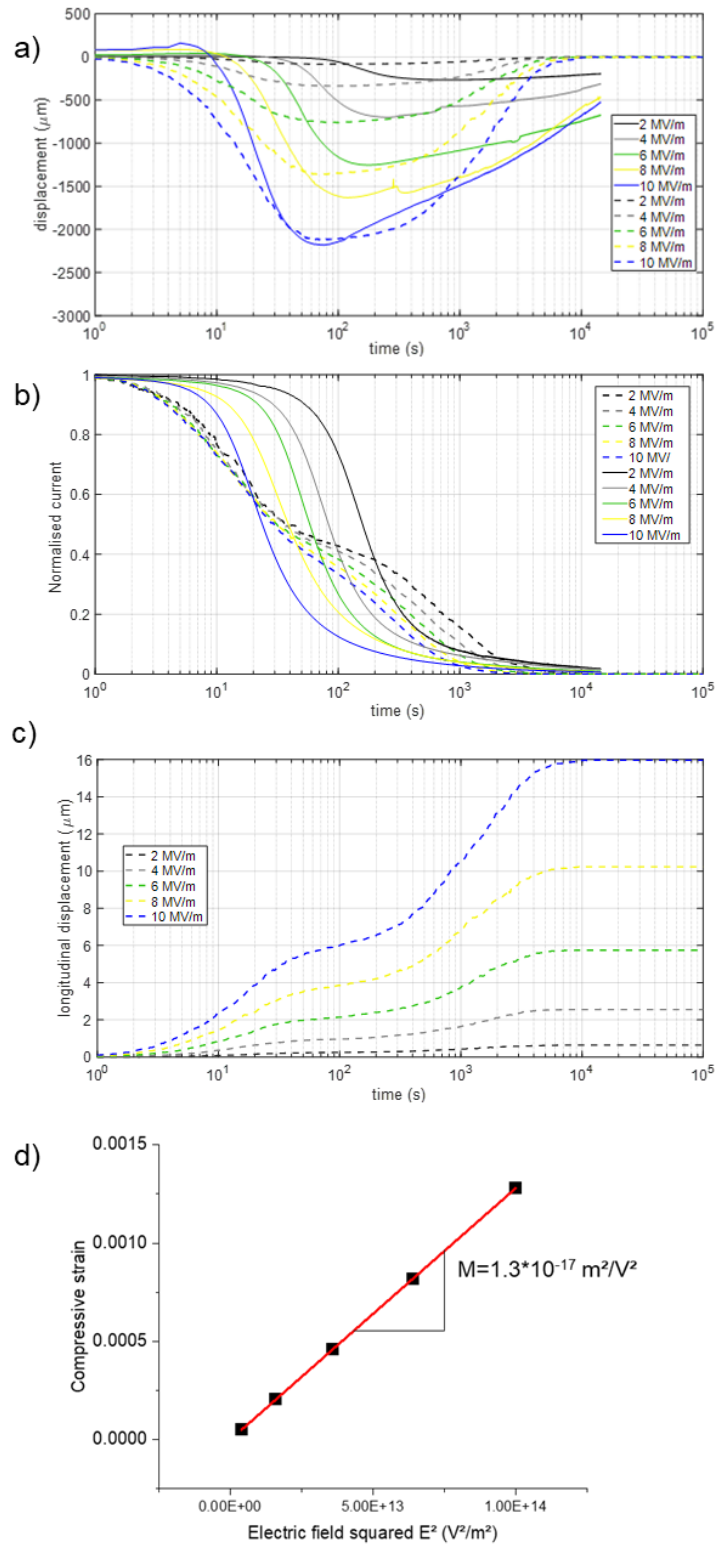


Figure 8: Preliminary simulation results (dashed line) versus experimental data (continuous line). a) Bending displacement as a function of time. b) Normalized electrical current as a function of time. c) Longitudinal extension of the sample as a function of time (simulation only). d) Calculated compressive strain as a function of electric field squared ( $E^2$ ).

340 Assuming that this elongation is isotropic in the yz plane, this leads to a decrease in thickness of  
341 0.1% (with a Poisson ratio of approximately 0.5). This can be compared with recently published data  
342 [8]: the corresponding electromechanical coefficient  $M$  obtained with the simulation is  $1.3 \times 10^{-17} \text{ m}^2/\text{V}^2$   
343 (figure 8d), which is among the wide range of values reported in literature. This shows that the charge  
344 carrier-based mechanism proposed here is very likely an important contributor to the electrostriction  
345 observed in this type of PU-based sample under parallel electrodes.

346 Although the simulations well reproduce the general characteristics of the experimental results such  
347 as (i) the order of magnitude of the four-decade time scale, (ii) the bending amplitude, and (iii) the  
348 current evolution, several differences are notable.

349 Because we did not consider possible changes in carrier mobility under a strong applied electric  
350 field [37] and also because the local electric field was introduced empirically, it appears that the times  $t_i$   
351 and  $t_d$  at which the bending deflection starts and the electric current drops do not depend on the applied  
352 field, contrary to the behavior exhibited by the samples.

353 Moreover, the experimental bending peaks are less symmetrical (on a logarithmic time scale) than  
354 the simulated curves. This could be because we have considered the particles to be initially randomly  
355 dispersed in the core domain. This is likely not the case because some of the carriers, if they are ions,  
356 could recombine with electrons to become atoms, especially near the electrodes. These assumptions will  
357 be studied in more detail in the future.

358

## 359 5. Conclusions

360 The complex kinetics of PU bending can last up to  $10^5$  s and is linked to the electric current. To our  
361 knowledge, this is the first time that measurements of both bending and current have been done  
362 simultaneously on PU for different applied electric fields over such a long time. This shows clearly  
363 that bending is the result of two processes with the same amplitude but different kinetics (the final  
364 displacement is zero). Qualitatively, the shape of the simulated curves agrees well with the  
365 experiments. However, the proposed simulation does not lead to an asymmetric bending curve, and the  
366 electric current is zero at the end of the simulation and initially too low compared with experiment.  
367 One way to improve the simulation would be to start with a heterogeneous particle distribution and  
368 take other mechanisms into account such as charge injection. The next step of this work in going from  
369 qualitative to quantitative simulation could be using a model material with controlled doping charges  
370 and determining parameters such as ionic mobility. A final and interesting point is that the resulting  
371 heterogeneous space charge density could also contribute to PU compression under an electric field,  
372 and consequently, its compression should be time-dependent with a kinetics occurring over five  
373 logarithmic decades of time in seconds.

374

375

376

377 Acknowledgments

378

379 The authors would like to acknowledge the financial support of the LyC Collaborative Research  
380 Project for the grant J21Ly18 and also the JSPS Core-to-Core Program (grant number:  
381 JPJSCCA20210005).

382

383 References

384

- 385 [1] Carpi F, Kornbluh R, Sommer-Larsen P and Alici G 2011 Electroactive polymer actuators as  
386 artificial muscles: are they ready for bioinspired applications? *Bioinspir. Biomim.* **6** 045006
- 387 [2] Bar-Cohen Y and Zhang Q 2008 Electroactive Polymer Actuators and Sensors *MRS Bull.* **33**  
388 173–81
- 389 [3] Pei Q, Pelrine R, Rosenthal M A, Stanford S, Prahlad H and Kornbluh R D 2004 Recent  
390 progress on electroelastomer artificial muscles and their application for biomimetic robots ed Y  
391 Bar-Cohen p 41
- 392 [4] Gu G, Zou J, Zhao R, Zhao X and Zhu X 2018 Soft wall-climbing robots *Sci. Robot.* **3**
- 393 [5] Tang C, Li B, Fang H, Li Z and Chen H 2018 A speedy, amphibian, robotic cube: Resonance  
394 actuation by a dielectric elastomer *Sensors Actuators A Phys.* **270** 1–7
- 395 [6] Javadi S and Razzaghi-Kashani M 2010 Dielectric elastomer actuators of silicone rubber-  
396 titanium dioxide composites obtained by dielectrophoretic assembly of filler particles ed Y  
397 Bar-Cohen p 76421E
- 398 [7] Diguet G, Cavaille J-Y, Sebald G, Takagi T, Yabu H, Suzuki A and Miura R 2021 Physical  
399 behavior of electrostrictive polymers. Part 1: Polarization forces *Comput. Mater. Sci.* **190**  
400 110294
- 401 [8] Yan Zhang, Véronique Perrin, Laurence Seveyrat L L 2020 On a better understanding of the  
402 electromechanical coupling in electroactive polyurethane *Smart Mater. Struct.* **29** 055007
- 403 [9] Kussmaul B, Risse S, Wegener M, Bluemke M, Krause J, Wagner J, Feller T, Clauberg K,  
404 Hitzbleck J, Gerhard R and Krueger H 2013 New DEA materials by organic modification of  
405 silicone and polyurethane networks ed Y Bar-Cohen p 86872S
- 406 [10] Wongtimnoi K, Guiffard B, Bogner-Van de Moortèle A, Seveyrat L, Gauthier C and Cavailié  
407 J-Y 2011 Improvement of electrostrictive properties of a polyether-based polyurethane  
408 elastomer filled with conductive carbon black *Compos. Sci. Technol.* **71** 885–92
- 409 [11] Diaconu I; and Dorohoi D . 2005 Properties of polyurethane thin films *J. Optoelectron. Adv.*  
410 *Mater.* **7** 921–4

- 411 [12] Jomaa M H, Masenelli-Varlot K, Diguët G, Seveyrat L, Lebrun L, Wongtimnoi K, Vechambre  
412 C, Chenal J M and Cavaillé J Y 2015 Modeling of segmented pure polyurethane  
413 electrostriction behaviors based on their nanostructural properties *Polymer (Guildf)*. **62** 139–47
- 414 [13] Kim B, Park Y D, Min K, Lee J H, Hwang S S, Hong S M, Kim B H, Kim S O and Koo C M  
415 2011 Electric actuation of nanostructured thermoplastic elastomer gels with ultralarge  
416 electrostriction coefficients *Adv. Funct. Mater.* **21** 3242–9
- 417 [14] Jomaa M H, Seveyrat L, Perrin V, Lebrun L, Masenelli-Varlot K, Diguët G and Cavaillé J Y  
418 2017 Difference between electrostriction kinetics, and mechanical response of segmented  
419 polyurethane-based EAP *Smart Mater. Struct.* **26** 035049
- 420 [15] Watanabe M, Wakimoto N, Shirai H and Hirai T 2003 Bending electrostriction and space-  
421 charge distribution in polyurethane films *J. Appl. Phys.* **94** 2494–7
- 422 [16] Watanabe M and Hirai T 2004 Space charge distribution in bending-electrostrictive  
423 polyurethane films doped with salts *J. Polym. Sci. Part B Polym. Phys.* **42** 523–31
- 424 [17] Lee A A, Colby R H and Kornyshev A A 2013 Electroactuation with single charge carrier  
425 ionomers: the roles of electrostatic pressure and steric strain *Soft Matter* **9** 3767
- 426 [18] Lin J, Liu Y and Zhang Q M 2011 Charge dynamics and bending actuation in Aquivion  
427 membrane swelled with ionic liquids *Polymer (Guildf)*. **52** 540–6
- 428 [19] Watanabe M, Kato T, Suzuki M, Amaike Y and Hirai T 1999 Bending Electrostriction in  
429 Polyurethanes Containing Ions as Contaminants or Additives *Jpn. J. Appl. Phys.* **38** L872–4
- 430 [20] Diaconu, I and Dorohoi D 2007 Electrostrictive response in polyurethane films containing  
431 lithium ionic impurities *J. Optoelectron. Adv. Mater.* **9** 990–3
- 432 [21] Iannarelli A, Ghaffarian Niasar M and Ross R 2020 Electrode interface polarization formation  
433 in dielectric elastomer actuators *Sensors Actuators, A Phys.* **312** 111992
- 434 [22] Sakamoto H and Yahagi K 1978 Relation between Electrostatic Capacity of Polyethylene and  
435 Electronic Space Charges Induced by High Field Application *Jpn. J. Appl. Phys.* **17** 1959–67
- 436 [23] Zhou Y, Wong Y W and Shin F G 2004 Mechanism of bending electrostriction in  
437 thermoplastic polyurethane *J. Appl. Phys.* **96** 294–9
- 438 [24] Barker R E 1976 Mobility and Conductivity of Ions in and into Polymeric Solids *Pure Appl.*  
439 *Chem.* **46** 157–70
- 440 [25] Wongtimnoi, K. (2011). *Polyuréthanes électrostrictifs et nanocomposites : caractérisation et*  
441 *analyse des mécanismes de couplages électromécaniques (Doctoral dissertation, INSA de*  
442 *Lyon).*

- 443 [26] Pissis P 2000 Structure–property relationships in proton conductors based on polyurethanes  
444 *Solid State Ionics* **136–137** 255–60
- 445 [27] Zhang Y, Seveyrat L and Lebrun L 2021 Correlation between dielectric, mechanical properties  
446 and electromechanical performance of functionalized graphene / polyurethane nanocomposites  
447 *Compos. Sci. Technol.* **211** 108843
- 448 [28] Watanabe M and Hirai T 2004 Bending-electrostrictive response of polyurethane films  
449 subjected to a reversed electric field *J. Appl. Polym. Sci.* **92** 3644–50
- 450 [29] Watanabe M and Hirai T 2004 Close Relationship between Bending-Electrostrictive Response  
451 and Space Charge Distribution in a Polyurethane Film *Jpn. J. Appl. Phys.* **43** 1446–8
- 452 [30] Montanari G C and Morshuis P H F 2005 Space charge phenomenology in polymeric  
453 insulating materials *IEEE Trans. Dielectr. Electr. Insul.* **12** 754–67
- 454 [31] Caponetto R, De Luca V, Graziani S and Sapuppo F 2013 An optimized frequency-dependent  
455 multiphysics model for an ionic polymer–metal composite actuator with ethylene glycol as the  
456 solvent *Smart Mater. Struct.* **22** 125016
- 457 [32] Bufalo G Del, Placidi L and Porfiri M 2008 A mixture theory framework for modeling the  
458 mechanical actuation of ionic polymer metal composites *Smart Mater. Struct.* **17** 045010
- 459 [33] Zhou F, Yang X, Xiao Y, Zhu Z, Li T and Xu Z 2020 Electromechanical analysis and  
460 simplified modeling of dielectric elastomer multilayer bending actuator *AIP Adv.* **10** 055003
- 461 [34] Roy S Le, Baudoin F, Laurent C and Teyssedre G 2020 Introduction of Ionic Contributions to  
462 a Charge Transport Model for Dielectrics *2020 IEEE 3rd International Conference on*  
463 *Dielectrics (ICD)* (IEEE) pp 509–12
- 464 [35] Timachova K, Watanabe H and Balsara N P 2015 Effect of molecular weight and salt  
465 concentration on ion transport and the transference number in polymer electrolytes  
466 *Macromolecules* **48** 7882–8
- 467 [36] Aziz S B, Woo T J, Kadir M F Z and Ahmed H M 2018 A conceptual review on polymer  
468 electrolytes and ion transport models *J. Sci. Adv. Mater. Devices* **3** 1–17
- 469 [37] Huang Y, Jämbeck J and Unge M 2017 Understanding the Ionic Conduction in Dielectric  
470 Polymers at High Electric Fields Using Molecular Dynamics Simulations *ACS Macro Lett.* **6**  
471 571–4
- 472